Materials and Design 165 (2019) 107582

Contents lists available at ScienceDirect

Materials and Design

journal homepage: www.elsevier.com/locate/matdes

Analysis of the tensile fracture properties of ultra-high-strength fiber-reinforced concrete with different types of steel fibers by X-ray tomography

José D. Ríos[a], Carlos Leiva[a], M.P. Ariza[a], Stanislav Seitl[b], Héctor Cifuentes[a,*]

[a] ETS Ingeniería, Universidad de Sevilla, Camino de los Descubrimientos, s/n, 41092 Sevilla, Spain
[b] Academy of Sciences of the Czech Republic, Institute of Physics of Materials, žižkova 22, Brno 616 62, Czech Republic

HIGHLIGHTS

- This work identifies the mechanisms involve in the micro-scale of UHSFRC and help to understand its macro-scopic behavior
- The addition of steel fibers to UHSFRC improved its microstructure, with a great dependence on the type of fibers
- A better alignment effect was obtained for long macro-fibers but the best flexural behavior was observed for micro-fibers
- The fibers addition improved the cracking strength of the matrix mainly due to the improvement produced in its microstructure
- A better tensile and fracture behavior with the lowest distortion of the matrix was obtained when short micro-fibers are used

GRAPHICAL ABSTRACT

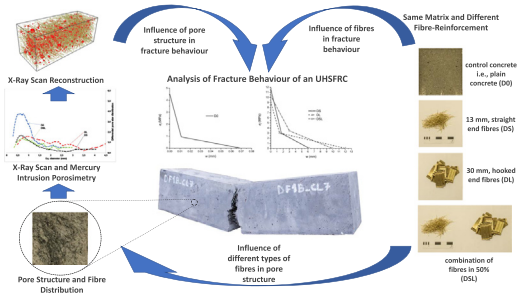

ARTICLE INFO

Article history:
Received 13 September 2018
Received in revised form 24 December 2018
Accepted 3 January 2019
Available online 7 January 2019

Keywords:
Ultra-high-strength concrete
X-ray computed tomography
Steel fibers
Concrete matrix
Tensile behavior
Fracture behavior

ABSTRACT

This study is concerned with the analysis of the tensile properties of an ultra-high-strength fiber-reinforced concrete manufactured with short and long steel fibers. The analysis involve using different techniques - from mechanical tests to X-ray computed tomography - to relate the observed variation of the mechanical properties of the mixes with their porosity. A comprehensive study of the porosity distribution was conducted on the basis of the analysis of X-ray computed tomography images and porosimetry. The study shows the influence of the type of fiber used in the reinforcement on the pore size and distribution of the concrete matrix and consequently on its tensile properties. The tensile properties are obtained with an inverse analysis method available in the literature that yielded the first-cracking tensile strength (f_t) and the ultimate tensile strength (f_{tu}) and related with the inner structure of the concrete matrix. Our results prove that the tensile properties, especially the first-cracking strength, vary depending on the fibers used. These findings help mix designers make a decision about the type of fibers that should be used when a high first-cracking tensile strength is needed and make it possible to quantify the effect of the fiber.

* Corresponding author.
E-mail address: bulte@us.es (H. Cifuentes).

https://doi.org/10.1016/j.matdes.2019.107582

1. Introduction

Fiber-reinforced concrete (FRC) is a cement-based material in which a high number of fibers - usually steel fibers for a better structural performance - are randomly dispersed on a cementitious matrix. Consequently, FRC is considered as a composite material in which the addition of fibers enhances the properties of the mix, especially its tensile and fracture properties, but can also generate voids and foster the nucleation and growth of microcracks inside the matrix. Several studies have demonstrated that the presence of fibers can affect to the inner structure of the matrix and its porosity [1-3]. Although most publications in this area of research show that the damage induced in the matrix can be related to the presence of fibers, a number of them show an opposite effect including a decrease in the porosity of the matrix for certain fiber contents [4]. This effect may be due to the fact that several factors associated to the fibers, such as their material, length and diameter have a relevant impact on the behavior of the FRC [5,6] and its influence on the concrete matrix is not yet clear. In a recent paper, Simoes et al. [7] reported that the presence of fibers modify the global behavior of the concrete matrix, whereas the fibers material becomes a determinant factor, controlling its strength and ductility. Moreover, in mixes with high fiber content, the porosity of may the concrete can increase during its manufacturing process, while the additional air bubbles generated mostly concentrated beneath the steel fibers, as observed by Hwang et al. [3] in mixes with a fiber content of 2.0% in volume fraction. This concentration could lead to a clear reduction in the effectiveness of fiber reinforcement due to the decrease of its interfacial bond strength. All these features relate to the influence that fibers have on the microstructure of the matrix and how it modifies the behavior of the material at the macro-scale. For these reasons, identifying and understanding the mechanisms that occur at the micro-scale due to the presence of fibers and their relationship with the macro-scale behavior is crucial. Although some papers relate the macro-scale properties with the micro-scale by using micromechanics models [8,9], the bibliography addressing a comprehensive experimental multiscale analysis is scarce.

In the case of ultra-high-strength fiber-reinforced concrete mixes (UHSFRC), their remarkable mechanical properties, such as compressive strength in excess of 200 MPa [10,11] and flexural strength above 30 MPa [12], are due to the very dense microstructure of its matrix [13] and the high steel fiber content (usually greater than 2.0% in volume). This ensures a better post-peak behavior of the concrete, provides a high degree of ductility [14] and enhances the fracture [14,15] and tensile [16,17] properties of the material. In some applications, such as prestressed concrete structures, where the cracking of the concrete must be thoroughly controlled, it is important to distinguish between the cracking strength of the matrix (f_t) and the ultimate or post-cracking strength (f_{tu}) of the FRC mix. Depending on the type of fibers used to reinforce the concrete and due to the nature of this type of materials, different values of f_t and f_{tu} can be obtained. The correct determination of these properties entails the use of inverse analysis methods based on empirical formulations [18] or cohesive models [19]. There is a relationship between these variables that strongly depends on the fibers. Albeit straight and short fibers are usually preferred to obtain better mechanical properties [20], hooked-end longer fibers are usually employed to reduce costs and enhance the strain capacity of the concrete [21]. In some circumstances, a combination of both straight and the hooked-end fibers is used to reduce costs and moderate the decrease of the mechanical properties. In a recent paper, Yoo et al. [22] conducted a comparative analysis of the flexural behavior of ultra-high-strength concrete reinforced with up to three different straight steel fibers (short, medium-length and long). However they did not consider hooked-end fibers, nor analyse the relationship between the obtained mechanical properties and the inner structure of the matrix.

Today, the use of micro X-ray computed tomography (XCT) to characterize engineered materials has become increasingly widespread because of the availability of XCT equipment in laboratories. This technique makes it possible to characterize the internal structure of the materials at several scales (from micro- to macro-scale), clearly showing the internal distribution of the components of the material, particularly those with different densities. There are several examples of its use to characterize metals and alloys [23,24], porous materials [25], ordinary composites [26] and fiber-reinforced composites [27] and asphalt mixtures [28]. In the case of concrete, due to its inherent porosity, the X-ray technique has been successfully applied to the study of plain concrete [29-33] as well as fiber-reinforced concrete [4, 34-37]. This technique is particularly helpful when steel fibers are used, due to the well-differentiated densities of the voids, fibers, aggregates and cementitious matrix [37] and it provides a powerful tool to analyse the distribution of fibers inside the matrix [38,37] or for the multiscale modeling of concrete [39]. In a very recent paper, Skarżyński and Suchorzewski [40] studied the mechanical and fracture properties of a normal-strength FRC by using XCT and related these properties with the microstructure of the concrete matrix. However, they measured the tensile strength of the concrete by means of splitting tests and they did not distinguish between the cracking strength of the cementitious matrix nor the ultimate tensile strength of the FRC. The utilization of XCT to characterize UHSFRC is less frequent [41,42] and not exempt from added difficulties due to the large amount of steel fibers present in these mixes [43]. However, coarse aggregates are usually avoided in this type of concrete in order to improve the packing of the matrix [44]. Therefore, efforts can focus only on the study of the air voids, the fibers and the cementitious matrix and not distinguish between the cement paste and aggregates.

In this research, we conducted a comprehensive multiscale experimental study about the influence of the type of steel fibers used to reinforce UHSFRC on the mechanical properties of the concrete, with especial emphasis on distinguishing between the cracking strength of the matrix and the tensile strength of the concrete, and their relationship with the change in the microstructure of the cementitious matrix using X-ray computed tomography and mercury intrusion porosimetry. Concrete reinforced with different fibers in shape, length and diameter was tested to determine its tensile and fracture properties and to relate the cracking and post-cracking strength of the mix with the fibers used to reinforce it and with the porosity of the matrix. Results confirm the applicability of X-ray computed tomography to provide useful information about the effect of the presence of fibers and to analyse aspects regarding the distribution of fibers inside the concrete, as well as the porosity and internal structure of the matrix. Our results, including different steel fibers, different geometric properties and economic cost, provide the means to carry out a thorough analysis of the properties and applications of this material in those cases of practical engineering where not only a high value of tensile strength of the material is required but also cracking strength.

2. Experimental program

The experimental program was designed to analyse the influence of the type of fibers (i.e., micro- or macro-fibers) used to reinforce the cementitious matrix, decoupling the behavior of the matrix from that of the fiber-reinforced concrete. The different UHSFRC mixes were designed to have the same matrix and different types of reinforcement (ranging from a mix reinforced with micro- or macro-fibers only to a hybrid reinforced concrete with a mixture of both fibers at 50%-50%.).

2.1. Materials

Four different mixes of ultra-high-strength fiber-reinforced concrete were prepared. As explained above, the mixes only differed

in the type of fibers used as reinforcement. The constituents of the matrix were the same for all mixes, as specified in Table 1. The UHSFRC mixes were designed and manufactured following the recommendations given in [45] in order to obtain self-compacting mixes. The binder materials were Type I Portland cement 52.5-SR produced by the Portland Valderribas cement factory (Seville, Spain), silica fume (SF) manufactured by SIKA and ground-granulated blast-furnace slag (GGBS) provided by Arcelor, Spain. The aggregates were two types of quartz sand with different maximum aggregate size. The finest sand had a maximum aggregate size of 0.315 mm while the coarsest one was below 0.800 mm. A third-generation polycarboxylic ether-based superplasticizer (MasterGlenium ACE 325) with a specific gravity of 1.04 manufactured by BASF was used.

Two different steel fibers were used in the analysis. Both were supplied by Bekaert (Belgium) and labelled as micro- and macro-fibers in our study. The micro-fibers were straight OL 13/.20, 13 mm in length and 0.20 mm in diameter. The macro-fibers were hooked-end Dramix RC80/30CP, 30 mm in length and 0.38 mm in diameter. The length of macro-fibers was limited in order to achieve good self-compactability of the mix reinforced with the longest fibers (DL).

The four UHSFRC mixes developed in this study were labelled as D0, DS, DL and DSL with the type of fibers and dosage specified in Table 2. The D0 mix without fibers was considered as the reference concrete matrix. The remaining mixes were fiber-reinforced and contained the same fiber content (2.5% in volume). Therefore, the difference between the fiber-reinforced mixes was only the type of fiber used as reinforcement. Specifically, the DS mix was reinforced only with micro-fibers, the DL mix contained macro-fibers, and the DSL mix was a hybrid reinforced concrete with both types of fibers, combined at 50%.

2.2. Specimen preparation and mechanical standard tests

Each of the fiber-reinforced mixes (DS, DL and DSL) was used to cast 4 beams (100 × 100 × 440mm^3), four cubes (100 × 100 × 100mm^3) and four cylinders (100 × 200mm^2). The various concretes were prepared in a vertical mixer. The coarsest constituent (i.e., coarse sand) and the finest one (i.e., SF or GGBS) were mixed first, followed by the next coarsest constituent (i.e., fine sand) and next the finest constituent (i.e., cement), and so on. Before each addition, the constituents were mixed for 2 min. The superplasticizer was added to the water in order to fluidize the dry mix. All constituents were mixed for at least 30 min to obtain the right consistency. After 24 h the specimens were unmolded and cured in water at ambient temperature for 28 days.

The compressive strength of all mixes was determined according to EN12390-3:2009 [46] from the cubic specimens. According to this standard, the loading rate was established as 0.5 MPa/s. The Young's modulus of concrete was determined according to EN12390-13:2014 [47] by gradually loading a cylindrical specimen in compression to approximately one third of its failure load. Two linear variable differential transformers (LVDTs) at 180° were used to measure the shortening of the distance between the machine platens and thus obtain the average strain undergone by the cylinders.

Table 1
Constituents of the matrix for the different UHSFRC mixes.

Constituent	kg/m^3
Cement (cm)	544
Silica fume	214
ggbs	312
Water (w)	188
Fine sand (<315 μm)	470
Coarse sand (<800 μm)	470
Superplasticizer (SP)	42
w/ cm	0.34
w/ binder	0.17

Table 2
UHSFRC mixes and fiber dosage.

Mix	Fiber type	Fiber dosage (kg/m^3)
D0	No fibers	0
DS	Micro-fibers	196
DL	Macro-fibers	196
DSL	Micro- (50%) and macro-fibers (50%)	196

2.3. Tensile and fracture behavior

2.3.1. UHSFRC (DS, DL and DSL mixes)

In reinforced concrete, a distinction must be made between its first cracking strength (related to the tensile strength of the matrix) and the ultimate tensile strength of the fiber-reinforced composite material, considering that the addition of fibers influences both strengths. For this reason, it is necessary to carry out an experimental study to determine these strengths separately. In a recent paper, López et al. [48] proposed a simplified inverse analysis method to determine the tensile properties of UHSFRC using unnotched four-point bending tests, distinguishing between first-cracking and tensile strength. In that study, the authors proposed a simplified method to obtain not only the tensile stress-strain (σ-ε) behavior prior to crack localisation (Fig. 1a), but also the stress-crack opening (σ-w) relationship after that point (Fig. 1b). This type of analysis provides a wealth of experimental information, so it was selected to determine the tensile properties of the fiber-reinforced mixes.

where σ_{75} and σ_{40} are the stresses corresponding to the points of intersection between the experimental σ_{fl}-δ curve, with $\sigma_{fl} = \frac{P}{W_{el}}$ (flexural strength), and the straight line that represents a secant stiffness of 75% and 40% of the initial stiffness(S_0), $\sigma_{loc} = 97\%\sigma_{max}$ (with σ_{max} as the peak flexural strength) is the cracking location point, δ_{75} and δ_{loc} are the experimental midspan vertical displacements corresponding to the points of σ_{75} and σ_{loc} respectively and δ_{80u} and δ_{30u} are the experimental displacements in the post-peak branch of the σ_{fl}-δ curve corresponding to the softening stresses of $\sigma_{80u} = 80\%\sigma_{loc}$ and $\sigma_{30u} = 30\%\sigma_{loc}$ respectively, $\varepsilon_{t.el} = \frac{f_t}{E}$, $\alpha = \frac{\varepsilon_{t.u}}{\varepsilon_{t.el}}$, $\beta = \frac{\varepsilon_{t.d}}{\varepsilon_{t.el}}$ and $\gamma = \frac{f_{t.u}}{f_t}$. For a more detailed explanation see [48] and [18].

Fig. 2a shows a drawing of the four-point bending tests carried out in this study with an indication of the main dimensions of the specimens. Fig. 2b shows a photograph taken during testing of one of the unnotched specimens. The tests were performed under displacement control at a loading rate of 0.5 mm/min in a closed-loop dynamic universal testing machine with a maximum load capacity of 200 kN. The vertical midspan deflection (δ) was measured by using a 50 mm LVDT transducer mounted on a rigid frame. The vertical deflection of the specimens during twisting was not measured as the supports had an anti-torque design. The use of a transducer with these characteristics makes it possible to record the full load-displacement curve until the specimen is broken into two halves. As shown, the S/D ratio was equal to 4; subsequently, following the inverse procedure proposed by López et al. [48], the values of the five key points to obtain the σ-ε curves had to be obtained by linear interpolation between the values provided in Table 3.

2.3.2. Unreinforced mix (D0)

The unreinforced mix (D0) was subjected to two different tests. To compare the value of the flexural strength of the plain concrete with that of the fiber-reinforced mixes, four-point bending tests were performed on unnotched D0 specimens. In this case, it was not possible to obtain a softening post-peak branch of the σ_{fl}-δ curve; however,

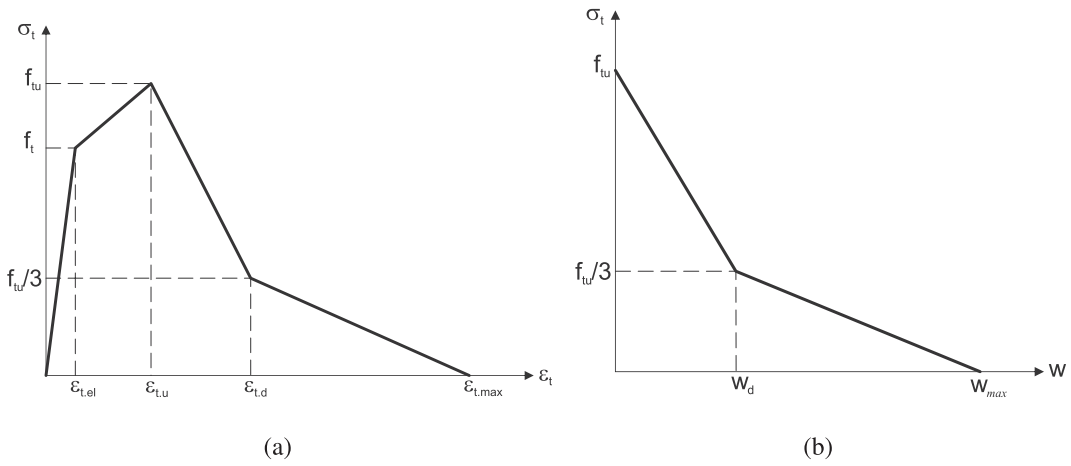

Fig. 1. Constitutive laws obtained from inverse analysis [48]: a) σ-ε law and b) cohesive σ-w law.

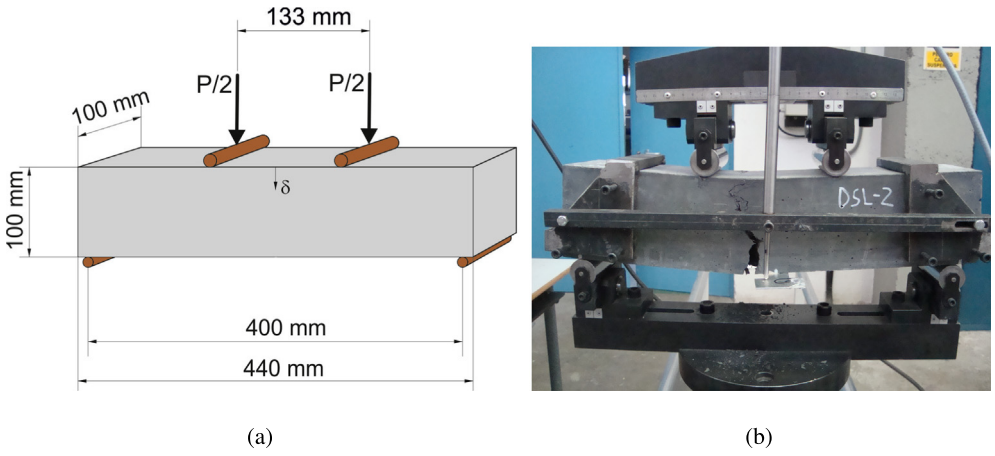

Fig. 2. Four-point bending test: a) drawing of the test with dimensions and b) photograph of one of the unnotched specimens during the test.

the flexural strength (i.e., modulus of rupture) was determined with the four point-bending test.

Three-point bending tests were also performed on notched specimens to determine the tensile and fracture properties of this type of concrete by means of flexural tests (Fig. 3a). This provided data on the fracture energy and bilinear tension softening law (σ-w) for plain concrete. These tests were performed according to the RILEM work-of-fracture method [49] applying the corrections proposed by Guinea et al. [50-52]. The tests were conducted controlling the crack mouth opening displacement (CMOD) with a clip gauge transducer. The midspan deflection was measured simultaneously with a LVDT transducer mounted on a rigid frame (Fig. 3b), as in the case of the four-point bending tests. All tests were performed with the same dynamic machine.

Table 3
Formulation of the inverse analysis procedure developed by López et al. [48].

Parameter	$S/D = 3$	$S/D = 4.5$
f_t	$\frac{\sigma_{75}}{1.63}(\frac{\sigma_{75}}{\sigma_{45}})^{0.19}$	$\frac{\sigma_{75}}{1.59}(\frac{\sigma_{75}}{\sigma_{45}})^{0.21}$
$\varepsilon_{t.u}$	$\frac{f_t}{E}(7.65\frac{\delta_{loc}}{\delta_{75}} - 10.53)$	$\frac{f_t}{E}(6.65\frac{\delta_{loc}}{\delta_{75}} - 9.40)$
f_{tu}	$\alpha^{-0.18}(2.46\frac{\sigma_{loc}}{\sigma_{75}} - 1.76)f_t$	$\alpha^{-0.17}(2.24\frac{\sigma_{loc}}{\sigma_{75}} - 1.55)f_t$
$\varepsilon_{t.d}$	$\gamma^{-0.37}\alpha^{-0.88}(3.00\frac{\delta_{80u}}{\delta_{loc}} - 1.80)\frac{f_t}{E}$	$\gamma^{-0.38}\alpha^{-0.89}(2.82\frac{\delta_{80u}}{\delta_{loc}} - 1.68)\frac{f_t}{E}$
$\varepsilon_{t.max}$	$2.81\beta^{-0.76}\gamma^{-0.19}\alpha^{1.42}(\frac{\delta_{30u}}{\delta_{loc}})^{1.85}\frac{f_t}{E}$	$2.17\beta^{-0.76}\gamma^{-0.26}\alpha^{1.48}(\frac{\delta_{30u}}{\delta_{loc}})^{1.86}\frac{f_t}{E}$
w_d	$w_0 + (\varepsilon_{t.d} - \varepsilon_{t.u} - \frac{2f_{tu}}{3E})\frac{S}{3}$	
w_{max}	$w_0 + (\varepsilon_{t.max} - \varepsilon_{t.u} - \frac{f_{tu}}{E})\frac{S}{3}$	

The fracture properties were determined with an inverse analysis based on the non-linear hinge model to obtain the key points of the bilinear tension softening diagram. The procedure is described in [53]. It should be noted that a value of the direct tensile strength of concrete (f_t) is obtained from the bilinear approximation of the tension softening diagram (Fig. 4).

2.4. Micro X-ray computed tomography and image analyses

Various prismatic core samples (100 × 25 × 25mm^3) were subjected to X-ray scans with the equipment of the X-ray laboratory of the University of Seville, Spain. The equipment consists of a Yxlon/Y Cougar Smt. system with a voltage range of 25–160 kV and a current range of 0.01–1.0 mA. The equipment can generate 2D and 3D images with a maximum geometric magnification of 2000×.

The core specimens were obtained from the 100 × 100 × 440mm^3 beams subjected to four-point bending tests. To avoid location effects on the porosity measurements (due to the concrete pouring into the molds), all the core specimens were obtained from the same part of the beam. Fig. 5 provides a diagram indicating the part from where the core specimens were taken.

The commercial software package VGStudioMax 2.2 was used for the 3D reconstruction of the images from the multiple 2D X-ray scanned radiographs, with a scanning resolution of 1024 × 1024 pixels. The beam hardening and ring effects [34,41] were minimized by post-processing of the images. Specifically, a smoothing

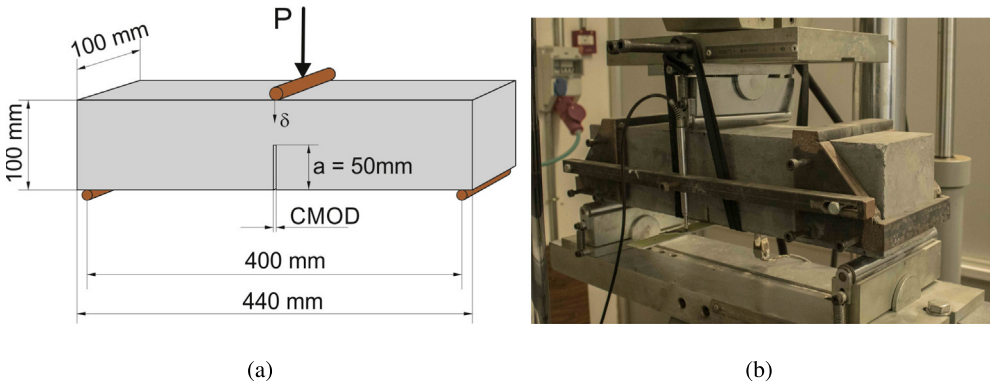

Fig. 3. Three-point bending test: a) drawing of the test with its dimensions and b) photograph of one of the notched D0 specimens during the test.

filter was applied to the data before the image analysis. One of the multiple 2D slices is shown in Fig. 6, where three main different shades of grey are distinguished in the grey-scale image. These shades are related to the different materials, depending on their density. The darkest shade corresponds to the lightest material (i.e., air voids or pores), the lightest shade shows the densest material (i.e., steel fibers) and the intermediate shade is that of the concrete matrix (with intermediate density).

To correctly identify the three main areas of interest (i.e., pores, steel fibers and matrix), it is necessary to determine the adequate grey-scale threshold [41]. This segmentation into different phases according to grey-scale thresholds and the post-data analyses was conducted using AVIZO commercial software. Fig. 7 shows the results obtained from the sensitivity analysis of the pore volume fraction according to the grey-scale threshold, as proposed by Qsymah et al. [41]. As shown by the figure, the relationship between the selected pore volume and the grey-scale threshold is linear for lower threshold values. The optimum value of the grey-scale threshold is that where the relationship starts to be non-linear, determined as the point where the difference with the linear regression trend is 5% (the grey-scale threshold is 12,000 in this example). Since scanning conditions can affect the absorption density and also the threshold values quantitatively, a sensitivity analysis was conducted for each sample to determine the optimum threshold in order to ensure the reliability of the results.

If the same procedure were followed to determine the optimal threshold of the pores for the steel fibers, there would be a severe

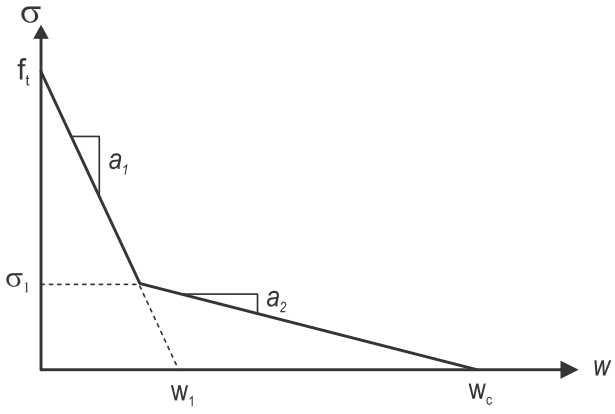

Fig. 4. Bilinear tension softening diagram.

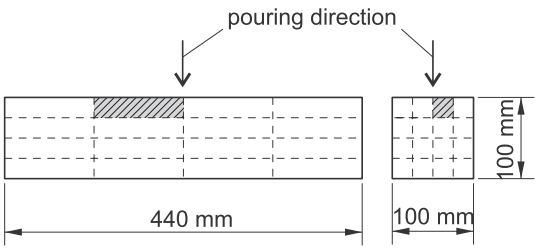

Fig. 5. Extraction of the core specimens from notched beams.

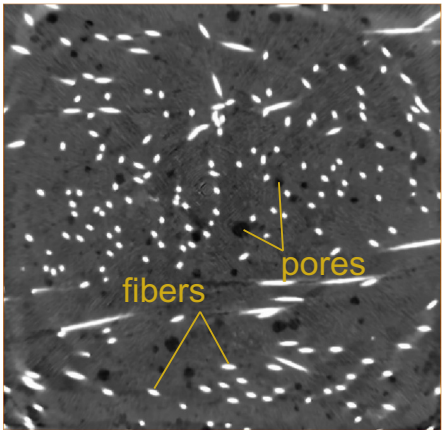

Fig. 6. Pore and fiber areas in a grey-scale CT scanned slice.

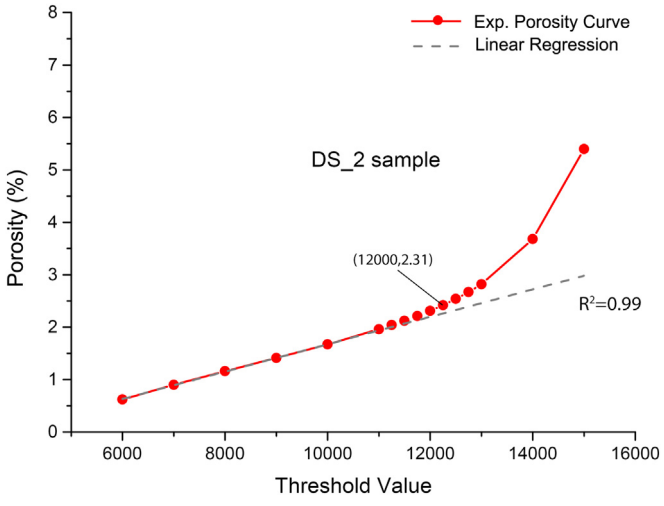

Fig. 7. Sensitivity analysis to determine which threshold value yielded a realistic volume fraction.

overlapping between nearby fibers, leading to errors (Fig. 8). For this reason, we proposed a new procedure to determine the optimum grey-scale threshold enabling the correct identification of the fibers. This procedure introduces the fiber content as a new variable. The optimum threshold for the fiber segmentation is that where the volume of fibers obtained from AVIZO matches that calculated as the number of fibers (not affected by the chosen threshold) multiplied by the unit volume provided by the fiber manufacturer. Following this procedure, a 3D sensitivity diagram (Fig. 9a) can be drawn for each segmented sample.

Fig. 9a shows three clearly identified stages. Stage 1 (A–B) corresponds to the start of the graph (at the end of the whitest tones) where the range of the grey-value threshold follows a linear trend. At this stage, the fiber volume increases while the fiber content decreases due to the merging of pixels inside each fiber area. Stage 2 (B–C) follows a 3D curvilinear progression with a lighter decrement of the number of fibers. This effect is produced because the fiber regions are almost completely selected and thus pixel merging is significantly reduced. Nevertheless, there is a new effect – fiber overlapping – that reduces the number of fibers more slowly. fiber overlapping occurs when some fibers are very close to each other and for a certain range of the grey-value threshold the fibers start to overlap. Finally, Stage 3 (C–D) follows a 2D curvilinear progression where the number of fibers detected is stabilised because the overlapping effect disappears and only the fiber volume (i.e., fiber thickness) increases because of a slight thickness increment. The 2D orthogonal projection (fiber Content-Porosity) shown in Fig. 9b demonstrates that the optimum threshold value (1570) is close to the loss of linearity (according to the end of Stage 1 and beginning of Stage 2). This point is obtained as the point where a deviation of the linear regression is below 0.1. This definition of the optimum threshold value was consistent in all the cases analysed (either pore or fiber segmentation), providing strong consistency and reliability to the proposed methodology.

2.5. High-pressure mercury intrusion porosimetry

High-pressure mercury intrusion porosimetry (MIP) was used to determine the porosity and pore size distribution in the range between 1 and 10,000 nm. For each mix (D0, DS, DL, and DSL), one sample 8 mm in diameter and 25 mm in length was tested. The

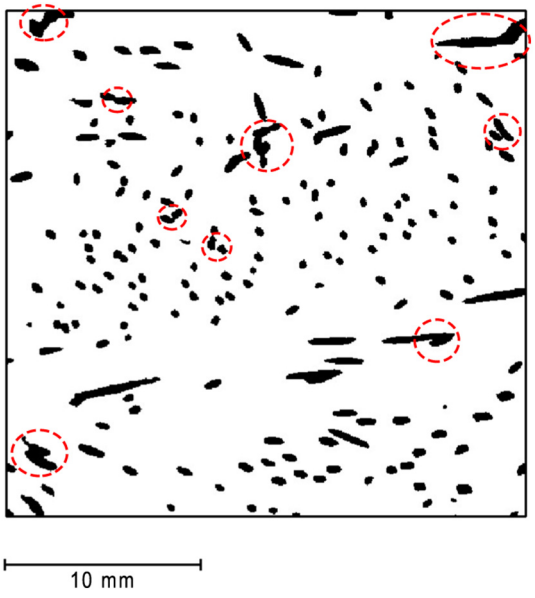

Fig. 8. Fiber overlapping due to an excessively high grey-scale threshold value.

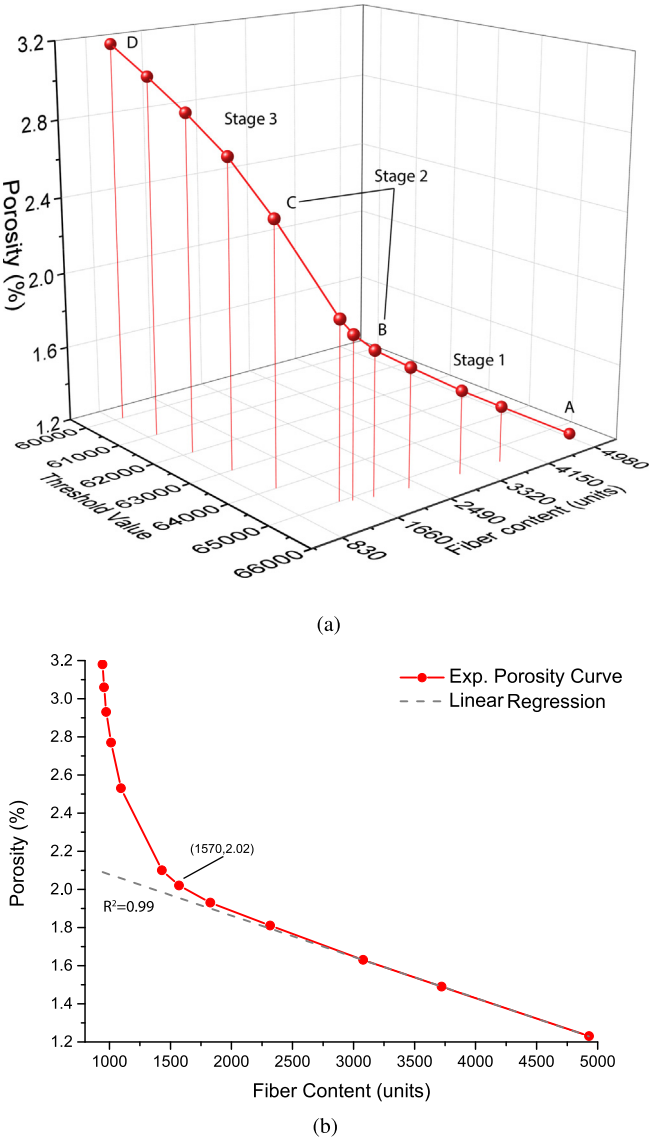

Fig. 9. Fiber sensitivity analyses proposed: a) 3D graph with the new parameter (i.e, fiber content); b) orthogonal projection of fiber content-porosity.

maximum applied pressure was 413 MPa; the contact angle was 140° and the surface tension was 480 mN/m. The samples for the MIP tests were also extracted from the upper part of the three-point bending specimens, from a nearby area to that where the samples for the X-ray analysis were taken.

3. Results and discussion

One of the main objectives of this study was to analyse the tensile fracture behavior of UHSFRC reinforced with different types of fibers and provide evidence of how such fibers affect the behavior of the matrix through the porosity generated at different scales (i.e. changes in its microstructure). The results of the porosity analysis are shown first so that the mechanical behavior obtained for the different mixes can be related to the effect of the steel fibers on the porosity of the matrix. Thus, a multiscale analysis of the effects of the addition of different fibers on UHSFRC is carried out, identifying the mechanisms involved at the micro-scale and understanding how they modify the macroscopic behavior of the UHSFRC mixes.

3.1. Porosity

The pore system in concrete consists of four types of pores: (a) gel pores, which are micropores whose characteristic dimensions are 0.5–10 nm; (b) capillary pores, which are mesopores with an average radius ranging from 5 to 5000 nm and correspond to the water-filled space between the original cement grains; (c) macropores due to deliberately entrained air; and (d) macropores due to inadequate compaction [54]. Gel pores do not adversely influence the strength of concrete [54]. By contrast, capillary pores and other larger pores are responsible for a reduction in strength and elasticity. In order to analyse the different pore sizes, larger pores are studied using X-ray computed tomography and capillary pores were explored with MIP. The results allow us to analyse the microstructure of these ultra-high-strength concretes and establish a comparison between them providing very useful information on how different fibers affect its behavior.

3.1.1. X-ray CT analysis

A comprehensive X-ray computed tomography analysis of all mixes was performed, making it possible to explore the porosity of a large volume of material (Fig. 5) at a scale of pore sizes ranging from 0.3 mm to several mm and providing detailed information about key factors of the pore distribution inside the matrix (e.g., pore size, location, sphericity). Fig. 10 shows some images obtained with the X-ray CT for each mix. The red spherical shaped volumes represent the pores and the golden lines represent the steel fibers.

As mentioned above, this technique enables an in-depth analysis of the large pores of the matrix (between 0.3 and 4.6 mm). Fig. 11 shows the cumulative and differential pore volume versus the equivalent diameter (Eq. diameter). The equivalent diameter represents the diameter of a sphere with the same volume of the pore and is defined as

$$d_{eq} = \sqrt[3]{6V_{pore}/\pi}, \tag{1}$$

where V_{pore} is the volume of a pore.

Fig. 11a reveals that porosity was highest in the D0 and decreased when different types of steel fibers were added, especially when DS and DSL fibers were used. It is important to highlight this aspect, since a high concentration of fibers did not produce a negative distortion in the matrix but rather improves its microstructure by reducing its porosity. D0 had a predominant equivalent diameter in the range of 0.5–1.3 mm; the distribution was much more uniform when the different types of steel fibers were used, although the number of larger pores was higher. Therefore, the presence of fibers induced pore concentration and thus increased pore size [3].

Additionally, Table 4 shows the most relevant parameters regarding the pore distribution analysis of the mixes, such as the average equivalent diameter, $\bar{d_{eq}}$, the total relative porosity, $\phi_{xr} = \frac{\sum V_{pore}}{V_{total} - \sum V_{fiber}}$, and the average sphericity, $\bar{\Psi}$, obtained from X-ray image analysis and defined as

$$\Psi = \frac{\pi^{1/3}(6V_{pore})^{2/3}}{A_{pore}}, \tag{2}$$

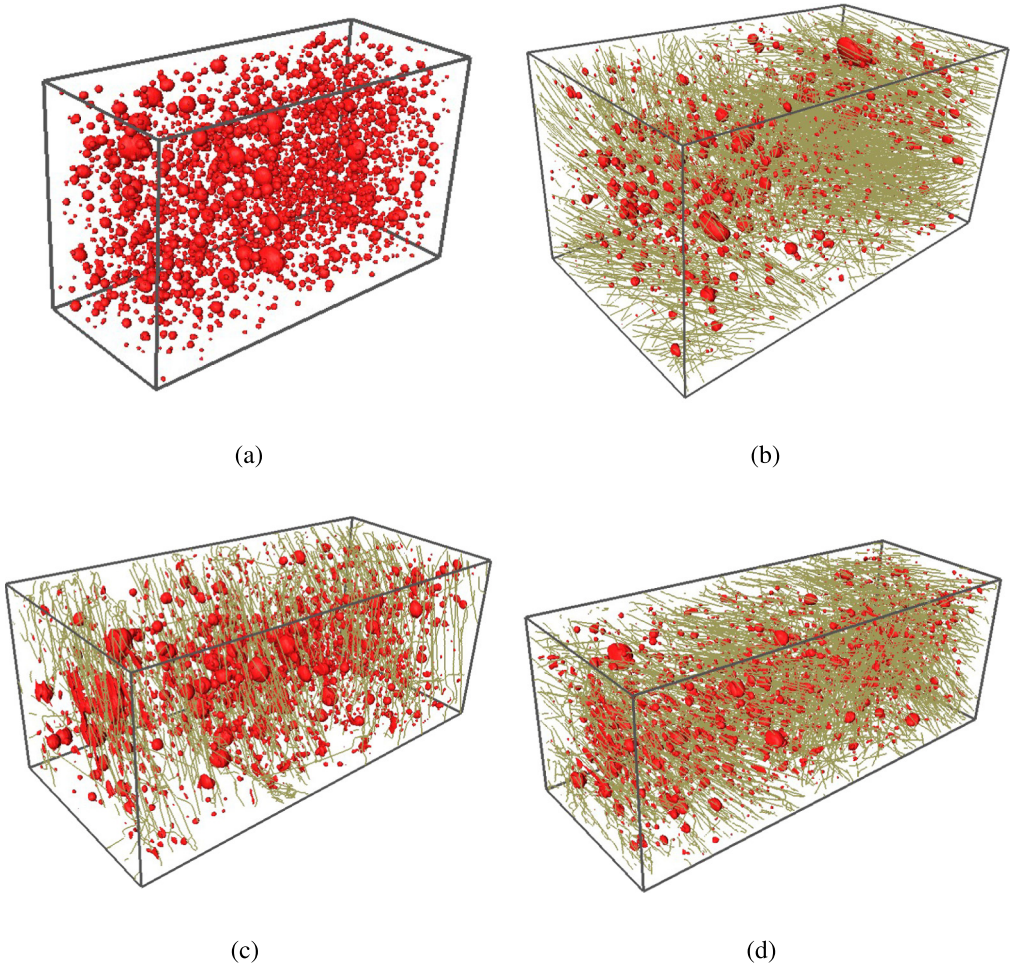

Fig. 10. X-ray CT image of the D0 (a), DS (b), DL (c) and DSL (d) mixes.

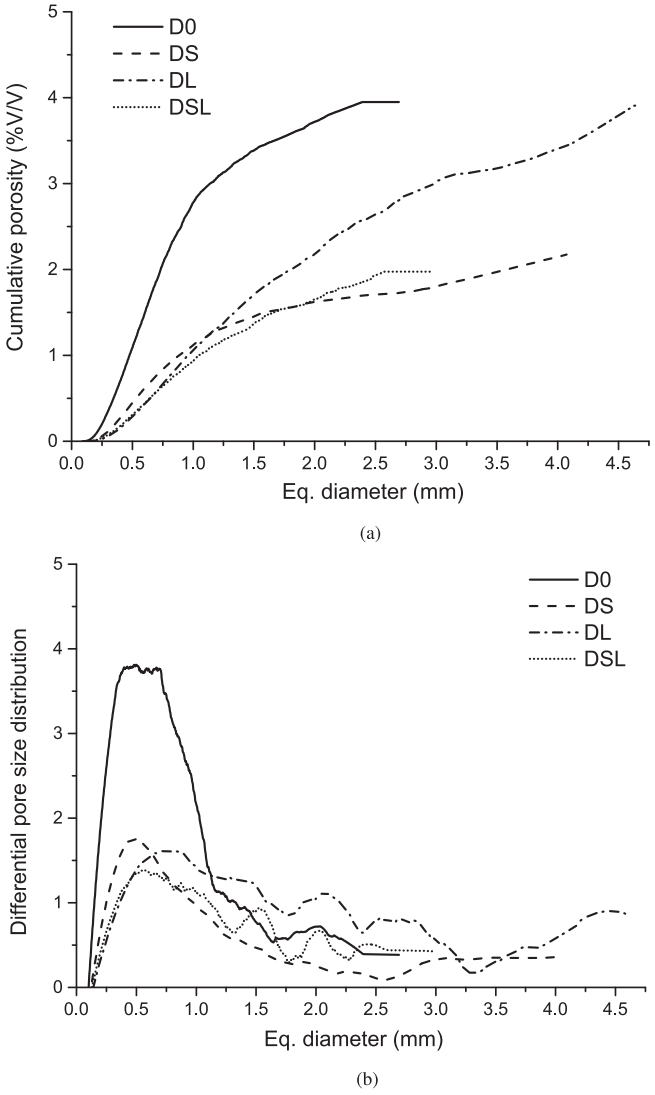

Fig. 11. Pore size distribution of mixes determined by X-ray CT. Cumulative (a) and (b) differential porosity curves.

where A_{pore} is the surface area of a pore. Sphericity represents how closely the shape of the pore is to a mathematically perfect sphere.

One of the most relevant effects observed in the analysis was the size of the pores, which increased with the presence of fibers. As observed in Fig. 11b, small-sized pores were more predominant in the unreinforced D0 mix than in the fiber-reinforced mixes. The average equivalent diameter (Table 4) increased with the presence of fibers, particularly in DL reinforced with the longest macro-fibers.

Most pores were clearly spherical, with values between 0.9 and 1. However, it was observed that the presence of fibers modified the shape of pores and reduced their sphericity. The greatest influence was produced by macro-fibers (i.e., DL) while micro-fibers (i.e., DS and DSL) showed an intermediate effect. As observed in Fig. 10, the pores in the fiber-reinforced mixes had a more marked oval shape. The lower sphericity of the pores was produced by the distortion of the matrix due to the fibers and related with the concentration of pores beneath the steel fibers, as reported by Hwang et al. [3] and confirmed by the X-ray image analysis conducted in our study.

Table 4
Porosity parameters obtained for each mix.

Property	D0	DS	DL	DSL
$\bar{d_{eq}}$ (mm)	0.28 ± 0.03	0.33 ± 0.01	0.44 ± 0.03	0.34 ± 0.02
$\bar{\Psi}$	0.93 ± 0.02	0.91 ± 0.01	0.84 ± 0.01	0.88 ± 0.01
ϕ_{xr} (%)	4.0 ± 0.9	1.9 ± 0.3	3.4 ± 0.8	2.2 ± 0.5

In this regard, Fig. 12 shows the CT image analysis of a transversal cross section of the DL specimens. As observed, there was a concentration of pores under the steel fibers with a lower sphericity. Moreover, the addition of fibers influenced the volume of pores generated in the matrix. The total porosity (ϕ_{xr}) was lower in the fiber-reinforced mixes. This means that the presence of fibers inside the cementitious matrix reduced its porosity: the fibers acted like tiny shovels helping to mix the concrete during its manufacturing inside the mixer, especially with the addition of micro-fibers. This effect was previously observed by Ponikiewski et al. [55], who reported a decrease in the porosity of the matrix in steel fiber-reinforced concrete with a high dosage of fibers. Simoes et al. [7] also obtained a slight decrease in the porosity of the matrix in some fiber-reinforced concrete mixes compared to the reference unreinforced matrix, especially in those with high fiber content. However, it should be noted that there is a lack of information in the literature regarding the analysis of the porosity of steel fiber-reinforced concrete mixes compared to their equivalent unreinforced mix, particularly in ultra-high-strength concrete. From our results, it is observed that the presence of fibers causes a drop of the total porosity of the matrix, as well as an increase in the average size of pores, a modification of the pores shape and a concentration of them beneath fibers, which clearly reflect changes on the microstructure of concrete due to the fibers. The modification of the microstructure must be related with changes in the macroscopic behavior of the mixes, as stated in the following sections.

3.1.2. Mercury intrusion porosimetry (MIP)

The MIP analysis provides useful information but can only be used for very small pores (between 0.003 and 30 μm), which complements the results obtained by X-ray CT, providing new results for smaller scales of the materials. Fig. 13 shows the pore size distribution obtained for all mixes (D0, DS, DL and DSL).

Results show that the unreinforced concrete (D0) had a significantly higher concentration of micropores with a size of about 0.01 μm, and the different types of steel fibers greatly decreased this peak. By contrast, the presence of fibers altered the porosity of the matrix, increasing micropore size (0.1 and 1 μm). These results are consistent with the conclusions obtained by Jiang at al. [2] and Hwang et al. [3], who used MIP and SEM techniques, respectively. The D0 mix had fewer pores between 0.1 and 1 μm than any type of fiber-reinforced mixes. In fiber-reinforced mixes, the highest amount of micropores

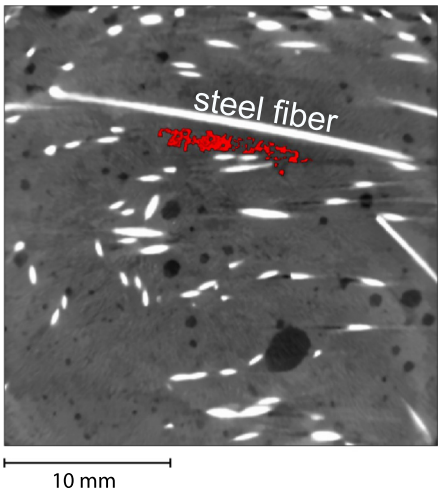

Fig. 12. X-ray image of a cross section of a DL specimen. Red pores have a sphericity factor lower than 0.3.

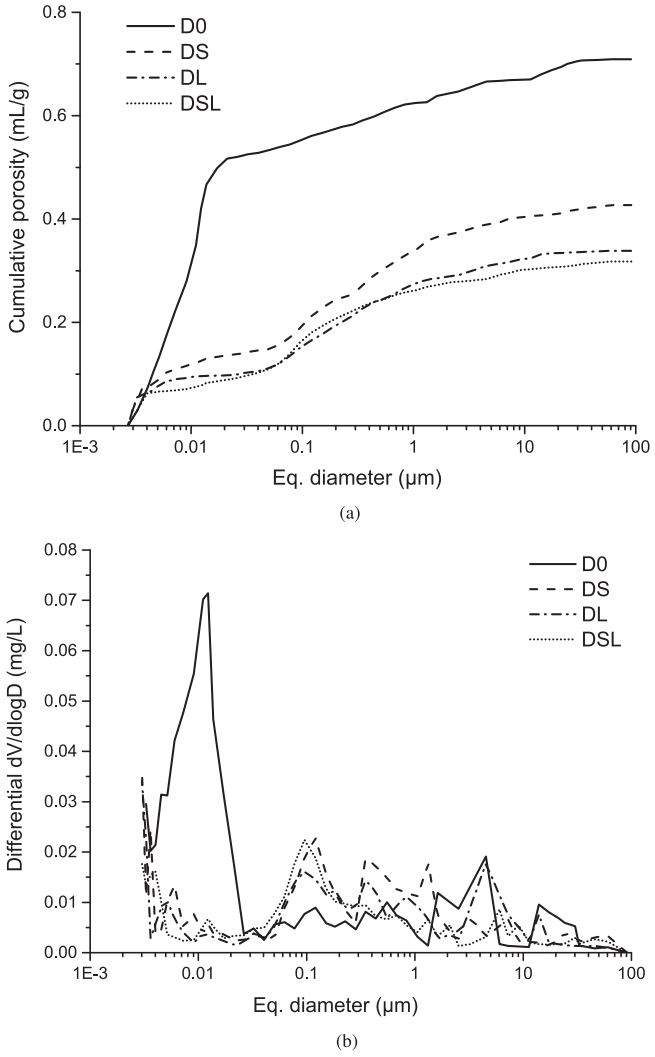

Fig. 13. Pore size distribution of mixes determined by MIP. Cumulative (a) and (b) differential porosity curves.

was observed in DS concrete; the lowest was found in the DL and DSL mixes (Fig. 13a). Again, these results support that the fibers modify the concrete matrix and limit its behavior at greater scales.

3.2. Analysis of the orientation and distribution of fibers

The distribution and orientation of steel fibers inside the matrix were also analysed using X-ray CT. Fig. 14 shows the histograms of the fiber orientation, θ and φ (see the reference coordinate system provided in Fig. 14c) obtained for each fiber-reinforced mix (DS, DL and DSL), where a predominant orientation of 0°, 90° and 180° was observed. Table 5 shows the average value of the orientation factors of the fibers, $\bar{\theta}$ and $\bar{\varphi}$, indicating the mean value and the coefficient of variation. Additionally, in order to study the fiber distribution inside the matrix, we counted the number of fibers observed in a transversal section of each scanned specimen. In this regard, Table 5 also shows the number of fibers per unit area of transversal cross section, n_f, obtained from X-ray CT image analysis. At least four transversal cross sections were analysed for each sample. The n_f data shown in Table 5 were obtained as the average value of all sections analysed and specimens for each mix.

A clear alignment effect was found in the macro-fibers [36], which were oriented parallel to the longest sides of the metal molds. By contrast, the orientation of the micro-fibers inside the matrix was more random but a slight alignment effect was still observed. These effects are shown by the orientation angles of the fibers θ and φ (Fig. 14). A greater alignment effect was considered for values of $\bar{\theta}$ closest to zero and values of $\bar{\varphi}$ closest to 90°. An intermediate behavior was observed in the blend of micro- and macro-fibers (i.e., the DSL mix). As expected, a greater number of fibers was observed in the transversal cross sections of the specimens made with the micro-fiber reinforced mix (i.e., DS). The lowest fiber values were found in the macro-fiber reinforced concrete (i.e., DL); an intermediate value of n_f was obtained in the DSL mix.

3.3. Compressive strength and Young's modulus

Fig. 15 shows the mechanical properties corresponding to well-established standardized tests, such as the compressive strength and Young's modulus obtained for the various UHSFRC mixes.

As shown in the figure, the presence of fibers led to a remarkable improvement in the compressive strength of the mixes, with an average increase of 17% of f_c when the fibers were added (similar to that reported by other authors under similar conditions [14]). This improvement was due to the positive sewing effect of the steel fibers against the tensile strains generated during the compression test in the concrete matrix [56]. As shown in Table 4, the lower the porosity values the higher the compressive strength.

The effects of the microstructure on the compressive strength of concrete have been widely studied by several authors in the past [57]. Most studies dealt with the determination of a relationship between compressive strength and porosity of the matrix, obtaining that a decrease in porosity leads to an increase in compressive strength, as expected. Thus, the increase of compressive strength obtained in this work for the UHSFRC with respect to the non-reinforced mix is due to the crack bridging effect of fibers and the reduction of the matrix porosity originated by the addition of fibers. As already mentioned above, our results confirm this fact, so that the values of the compressive strength are greater for the fiber-reinforced mixes and inversely proportional to the value of their porosity [58] (see Fig. 15).

With regards to the Young's modulus, we did not observe a clear influence of the presence of fibers on this parameter (Fig. 15), in agreement with previous results obtained by other authors [59]. This parameter is mainly influenced by the existence of a large number of pores with sizes in the order of nanometers, rather than by the existence of a smaller number of pores with sizes in the order of millimeters [60]. As can be observed in Figs. 11 and 13, the addition of steel fibers especially modifies the structure of the matrix at the micro-scale so a similar value of E_c was obtained for all mixes, even for the unreinforced mix (i.e., D0).

3.4. Tensile and fracture properties

3.4.1. Flexural strength

The flexural strength, f_{fl} (also known as modulus of rupture), of each concrete mix was obtained from the four-point bending tests. Fig. 16 shows the mean values and the deviation obtained for each mix.

As expected, a clear influence of the fibers was found regarding the flexural behavior of the mixes [61]. Mixes reinforced only with micro-fibers (DS) and those reinforced with hybrid micro- and macro-fibers (DSL) exhibited the best behavior, with a similar maximum value above 20 MPa. Even in the use of macro-fibers (DL mix), where the lowest value was obtained, the flexural strength was more than three times that obtained for the unreinforced mix (D0). Despite the fact that macro-fibers present a better alignment and an increase in the flexural strength of DL mix could be expected according to [62],

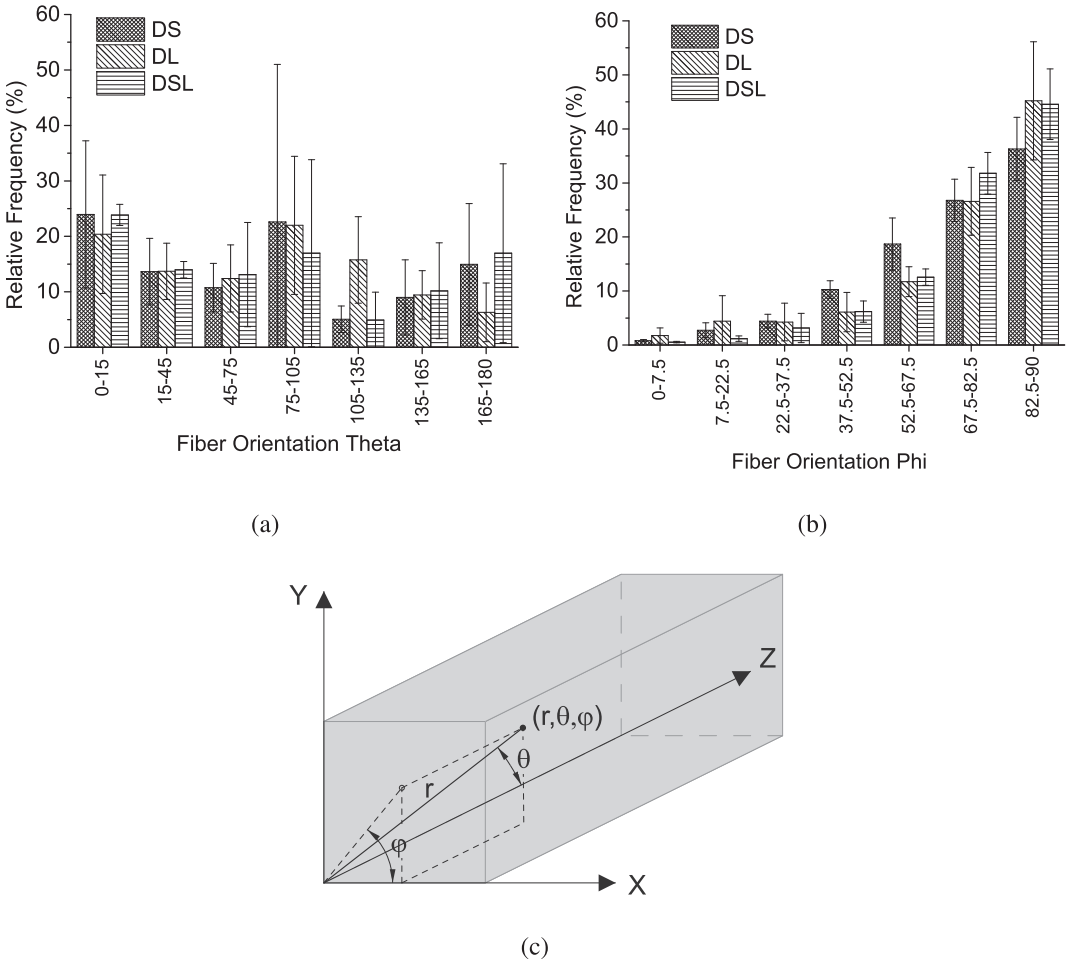

Fig. 14. Histogram of the fiber orientation for theta (a) and phi (b) according to the reference coordinate system indicated in (c).

the higher fiber density in the matrix that occurs when using micro-fibers produces a greater increase in the flexural behavior of DS and DSL mixes [63].

3.4.2. Constitutive σ-ε law of UHSFRC mixes in tension

The tensile stress-strain (σ-ϵ) curves for each of the fiber-reinforced mixes were obtained according to the inverse method proposed by López et al. [48] (Fig. 17a). With the aim of facilitating the comparison of the tensile behavior between the different mixes, Fig. 17b shows the first-cracking strength (f_t) and tensile strength (f_{tu}) values of all mixes.

As expected, the tensile strength, f_{tu}, of the fiber-reinforced mixes increased with flexural strength. The highest tensile strength value was obtained for the DS mix, reinforced only with micro-fibers. The values were quite similar in the DL and DSL mixes. Considerable differences were found between mixes in first-cracking strength. The highest value of f_t was obtained again for the DS mix, reinforced with micro-fibers; it amounted to 1.96 times the value obtained for the D0 mix. Nevertheless, the poorest value for the fiber-reinforced mixes was obtained for the DL mix, reinforced with only long fibers, and amounted to 1.45 times the value obtained for D0. In the DSL mix, results were intermediate between those of the DS and DL mixes. As observed, the presence of fibers improved the first-cracking strength,

Table 5
Mean value of the average orientation factors of fibers and number of fibers per unit area of the transversal cross section.

Mix	DS	DL	DSL
$\bar{\theta}^{(o)}$	37 ± 6	19 ± 4	29 ± 10
$\bar{\varphi}^{(o)}$	70 ± 1	72 ± 8	75 ± 4
$\frac{n_f}{cm^2}$	30 ± 5	7 ± 3	18 ± 7

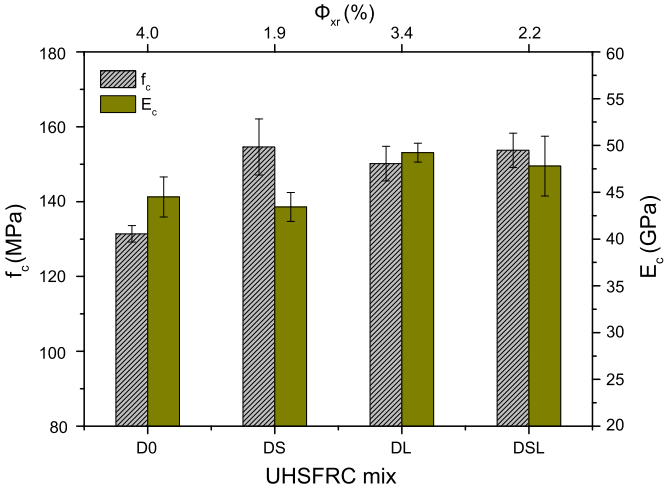

Fig. 15. Compressive strength and Young's modulus of UHSFRC mixes.

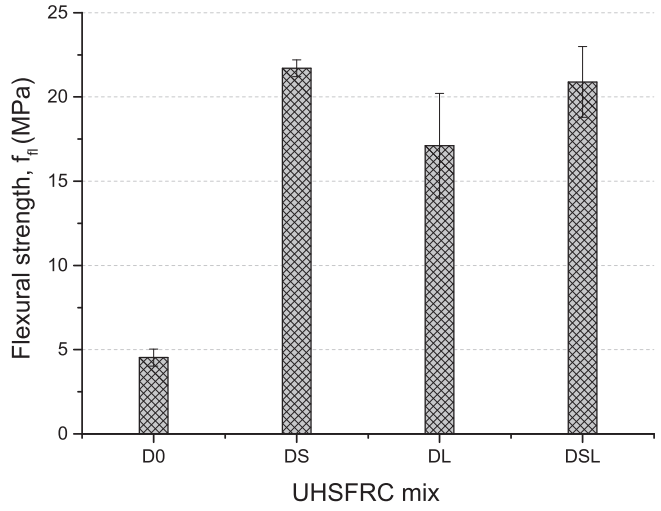

Fig. 16. Flexural strength of UHSFRC mixes.

f_t, of the matrix and the tensile strength, f_{tu}, of the composite concrete (cementitious matrix + steel fibers) with two effects. The first effect was due to the well-known mechanisms of crack trapping and bridging [64] of fibers; the second effect was related to the influence of fibers on the microstructure of the matrix. Overall, as shown by the X-ray CT analysis, fiber addition was associated with a decrease in the porosity of the cementitious matrix and a distortion in pore size and shape (i.e., the average equivalent diameter increased and the sphericity factor decreased). However, in the case of the macro-fibers the distortion of the matrix was the greatest obtained for the fiber-reinforced mixes (see Table 4), what explains the drop in the first-cracking strength obtained in the DL mix compared to DS and DSL mixes. In this mix, porosity was greater than in mixes with micro-fibers, pore size was larger and the sphericity factor was lower (Table 4). Specifically, the mix reinforced with long macro-fibers exhibited a worse cracking behavior. The first-cracking strength of the DL mix was still higher than that of the reference D0 mix because of the positive effect of fibers explained above. The best cracking behavior was obtained in the DS mix because of the very low porosity of the cementitious matrix and the larger number of fibers per area of the transversal cross-section in this mix [65] (Table 5). The porosity obtained for this mix was even lower than that of the D0 reference mix. It seems that steel fibers contribute to the mixing of concrete, acting as small micro-blades that help to beat the concrete matrix during the mixing, especially in the case of micro-fibers.

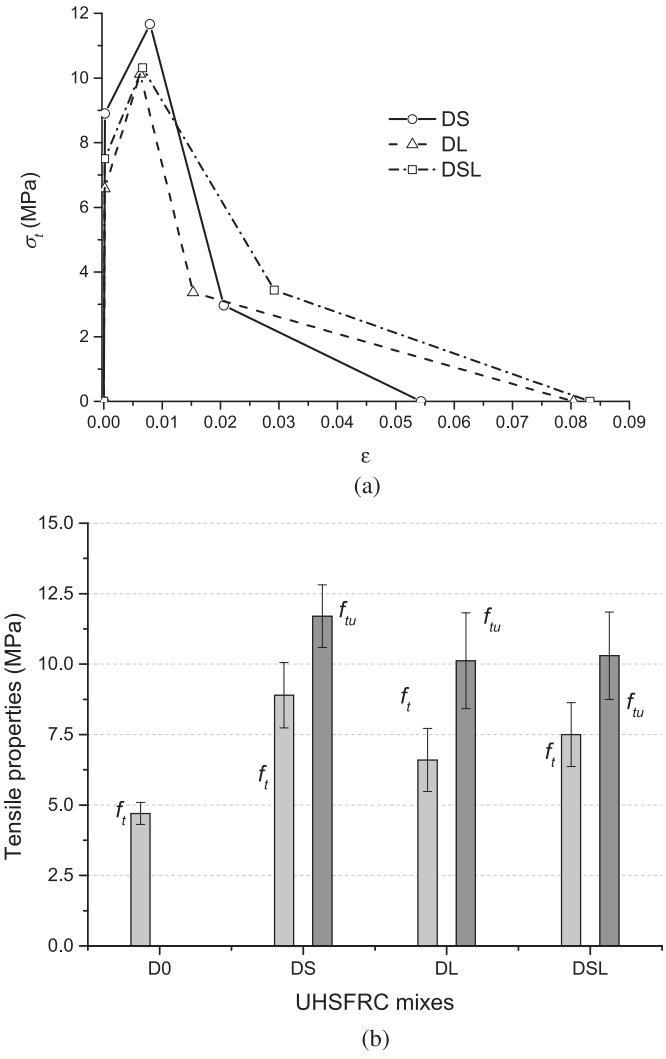

Fig. 17. σ-ε constitutive laws obtained for the fiber-reinforced mixes DS, DL and DSL (a) and tensile properties f_t and f_{tu} for all mixes (b).

3.4.3. Fracture energy and characteristic length

In the plain concrete (D0), its size-independent fracture energy was determined according to the RILEM work-of-fracture method and with the corrections proposed by Guinea et al. [50-52].

According to this method, the specific fracture energy of the plain concrete mix was determined as follows:

$$G_F = \frac{W_{F.M} + W_{F.NM}}{A_{lig}} \tag{3}$$

where $W_{F.M}$ is the measured work-of-fracture (area under the measured load-displacement curve) after the corrections of the initial part of the P-δ curve, $W_{F.NM}$ is the non-measured work-of-fracture, determined by adjusting the tail of the softening branch of the curve and $A_{lig} = B(D - a_0)$ is the ligament area.

Additionally, the bilinear tension softening diagram (σ-w) for the unreinforced D0 mix was also obtained according to the hinge model described in [53] and shown in Fig. 18a.

In the fiber-reinforced mixes (DS, DL and DSL), the specific fracture energy was calculated as the area under the cohesive σ-w laws [66]. These laws were obtained according to the procedure proposed by López et al. [18] (summarized in Table 3) and shown in Fig. 18b for comparison (the axis scales are not the same in both figures because of the large difference between the values of the displacements of the plain concrete and the fiber-reinforced mixes). The mechanisms involve in the fracture processes of UHSFRC are not exactly the same as in case of normal plain concrete due to the absence of coarse aggregates and the presence of steel fibers in the reinforced mixes. Nevertheless, cohesive models are also valid for this kind of concrete [70] and, although the whole σ-w diagram is influenced by fibers, the first linear branch of the softening diagram is more related with the microcracking of the matrix [69] while the second linear branch is mainly governed by the pullout of fibers [70].

As expected, the crack bridging effect of fibers [9,67] greatly increased the value of G_F [14] compared to that of the D0 unreinforced mix. The lowest value of the fiber-reinforced concrete mixes was obtained for DS, reinforced with micro-fibers, due to its lower length and diameter and consequently its lowest interfacial bond with the cementitious matrix [59]. For the mix reinforced with only long fibers, DL, the highest value of the critical opening displacement (w_c in Fig. 4) was obtained, due to the greater adherence of the fibers to the matrix [68]. However, the highest value of the fracture energy was obtained for the concrete reinforced with hybrid fibers, DSL, because it combines the favorable effects of the two types of

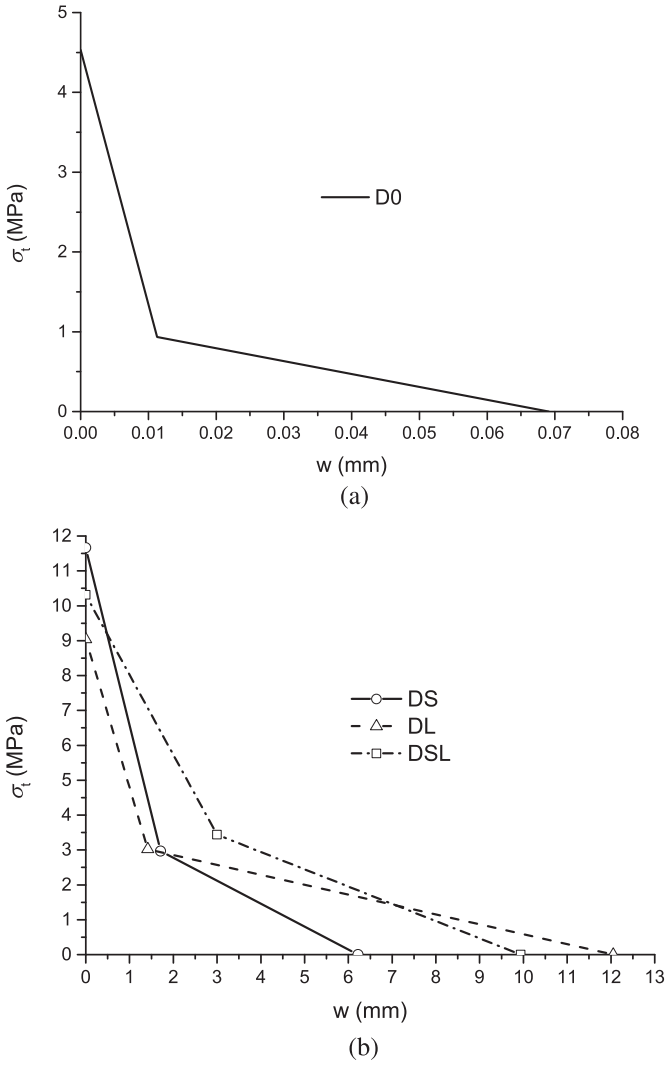

Fig. 18. Bilinear tension softening diagram for fiber-reinforced DS, DL and DSL (a) and unreinforced D0 (b) mixes.

fibers. On the one hand, the presence of short micro-fibers improves the behavior of the matrix, reducing its porosity with respect to the use of macro-fibers and increasing the toughening effect of fibers on the matrix [64], which increases its cracking strength. This effect is revealed in the bilinear softening diagram by a higher value of the initial fracture energy ($G_f = 1/2 f_t w_1$) enclosed by the first linear branch of the diagram (Fig. 4) [69]. On the other hand, the presence of long macro-fibers improves their adherence to the matrix, which provides a greater deformability to the material and increases the energy enclosed by the second branch of the bilinear softening law (G_F-G_f) [70] with respect to the one corresponding to the concrete reinforced with only short fibers.

Another important fracture parameter is the characteristic length, defined by Hillerborg [71] and given by

$$l_{ch} = \frac{G_F E_c}{f_{tu}^2} \tag{4}$$

Table 6 shows the values of the specific fracture energy and characteristic length obtained for each mix.

As the size of all specimens was the same, it was possible to conduct a ductility analysis directly based on the results of the characteristic length [72], so that the greater l_{ch}, the greater the ductility of the mix. Again, the highest ductile behavior was obtained for DSL mix, mainly due to its highest specific fracture energy value. By contrast, the most brittle behavior was shown by the unreinforced concrete, as its G_F value was much lower.

Table 6
Fracture energy and characteristic length.

Mix	G_F (N/m)	l_{ch} (mm)
D0	$64 \pm 8\%$	128
DS	$19,204 \pm 13\%$	6093
DL	$24,614 \pm 17\%$	11,832
DSL	$32,552 \pm 15\%$	14,667

4. Conclusions

The following conclusions can be drawn from the results:

- A clear influence of fibers on the microstructure of the ultra-high strength concretes was observed. In the UHSFRC explored in this study, with a particular content of steel fibers, we observed a reduction in the porosity of the cementitious matrix produced by fibers. Fibers act as tiny shovels that help to mix the concrete during its manufacturing and reduce its porosity.
- Improvement on the compressive strength of the reinforced mixes with respect to the unreinforced mix (i.e., D0), being the increase proportional to the reduction in their porosity. In case of the Young's modulus, it was not observed a clear effect of the addition of fibers, obtaining very similar values for all the mixes.
- The tensile properties of the UHSFRC mixes analysed depended on the type of fibers used as reinforcement. Although this conclusion may seem obvious, a distinction should be made between the first-cracking strength and the ultimate tensile strength. The maximum tensile strength of the mixes, f_{tu}, was quite similar regardless of whether the fibers used to reinforce them were macro- (35/0.55) or micro-fibers (13/0.2). However, the first-cracking strength, f_t, of the mixes was greatly influenced by the type of the fibers. The highest f_t values were obtained when short fibers were used, due to the greatest number of fibers crossing a unit sectional area of the matrix but also because of the influence of fibers on the porosity of the matrix.
- A better fracture behavior was obtained for the hybrid reinforced mix (50% of micro- and 50% of macro-fibers) due to the increase of the cracking strength of the matrix by the presence of micro-fibers and the greater deformations before the debonding of the macro-fibers.
- From a mechanical point of view, the best behavior was obtained by the mix reinforced only with micro-fibers. However, the higher price of this type of fibers can make it interesting to use a hybrid reinforced mix, which exhibited a better mechanical behavior than the mix reinforced only with macro-fibers but whose price is lower than that of mixes with micro-fibers only and its fracture behavior is better.

5. Data availability statement

All raw data reported in this paper is contained within the manuscript.

CRediT authorship contribution statement

José D. Ríos: Data curation, Formal analysis, Methodology, Validation, Writing - original draft, Writing - review & editing. **Carlos Leiva:** Data curation, Formal analysis, Methodology, Validation, Writing -

original draft. **M.P. Ariza:** Formal analysis, Investigation, Validation, Writing - original draft, Writing - review & editing. **Stanislav Seitl:** Formal analysis, Validation, Visualization, Writing - original draft. **Héctor Cifuentes:** Conceptualization, Investigation, Resources, Supervision, Writing - original draft, Writing - review & editing.

Acknowledgments

The authors would like to acknowledge the financial support provided to this study by the Spanish Ministry of Economy and Competitiveness under projects BIA2016-75431-R and DPI2015-66534-R and the Czech Sciences Academy under project No. 16-18702S.

References

[1] E. Poveda, G. Ruiz, H. Cifuentes, R. Yu, X. Zhang, Influence of the fiber content on the compressive low-cycle fatigue behavior of self-compacting SFRC, Int. J. Fatigue 101 (2017) 9–17. https://doi.org/10.1016/j.ijfatigue.2017.04.005.
[2] C. Jiang, K. Fan, F. Wu, D. Chen, Experimental study on the mechanical properties and microstructure of chopped basalt fibre reinforced concrete, Mater. Des. 58 (2014) 187–193. https://doi.org/10.1016/j.matdes.2014.01.056.
[3] J.P. Hwang, M. Kim, K.Y. Ann, Porosity generation arising from steel fibre in concrete, Constr. Build. Mater. 94 (2015) 433–436. https://doi.org/10.1016/j.conbuildmat.2015.07.044.
[4] T. Ponikiewski, J. Katzer, X-ray computed tomography of fibre reinforced self-compacting concrete as a tool of assessing its flexural behaviour, Mater. Struct. 49 (6) (2016) 2131–2140. https://doi.org/10.1617/s11527-015-0638-y.
[5] N. Buratti, C. Mazzotti, M. Savoia, Post-cracking behaviour of steel and macrosynthetic fibre-reinforced concretes, Constr. Build. Mater. 25 (2011) 2713–2722. https://doi.org/10.1016/j.conbuildmat.2010.12.022.
[6] S. Wang, M. Zhang, S. Quek, Mechanical behavior of fiber-reinforced high-strength concrete subjected to high strain-rate compressive loading, Constr. Build. Mater. 31 (2012) 1–11. https://doi.org/10.1016/j.conbuildmat.2011.12.083.
[7] T. Simoes, H. Costa, D.D. da Costa, E. Júlio, Influence of fibres on the mechanical behaviour of fibre reinforced concrete matrixes, Constr. Build. Mater. 137 (2017) 548–556. https://doi.org/10.1016/j.conbuildmat.2017.01.104.
[8] Y. Lee, S. Kang, J. Kim, Pullout behavior of inclined steel fiber in an ultra-high strength cementitious matrix, Constr. Build. Mater. 24 (2010) 2030–2041. https://doi.org/10.1016/j.conbuildmat.2010.03.009.
[9] V. Li, H. Stang, H. Krenchel, Micromechanics of crack bridging in fibre-reinforced concrete, Mater. Struct. 26 (1993) 486–494. https://doi.org/10.1007/BF02472808.
[10] B. Graybeal, Compressive behavior of ultra-high-performance fiber-reinforced concrete, ACI Mater. J. 104 (2) (2007) 146–152. https://doi.org/10.14359/18577.
[11] K. Wille, A. Naaman, G. Parra-Montesinos, Ultra-high performance concrete with compressive strength exceeding 150 MPa (22 ksi): a simpler way, ACI Mater. J. 108 (1) (2012) 1–11. https://doi.org/10.14359/51664215.
[12] R. Yu, P. Spiesz, H. Brouwers, Mix design and properties assessment of ultra-high performance fibre reinforced concrete (UHPFRC), Cem. Concr. Res. 56 (2014) 29–39. https://doi.org/10.1016/j.cemconres.2013.11.002.
[13] M. Reda, N. Shrive, J. Gillott, Microstructural investigation of innovative UHPC, Cem. Concr. Res. 29 (3) (1999) 323–329. https://doi.org/10.1016/S0008-8846(98)00225-7.
[14] K. Voit, J. Kirnbauer, Tensile characteristics and fracture energy of fiber reinforced and non-reinforced ultra high performance concrete (UHPC), Int. J. Fract. 188 (2014) 147–157. https://doi.org/10.1007/s10704-014-9951-7.
[15] N. Tran, T. Tran, J. Jeon, J. Park, D. Kim, Fracture energy of ultra-high-performance fiber-reinforced concrete at high strain rates, Cem. Concr. Res. 79 (2016) 169–184. https://doi.org/10.1016/j.cemconres.2015.09.011.
[16] S. Pyo, K. Wille, S. El-Tawil, A. Naaman, Strain rate dependent properties of ultra high performance fiber reinforced concrete (UHP-FRC) under tension, Cem. Concr. Compos. 56 (2015) 15–24. https://doi.org/10.1016/j.cemconcomp.2014.10.002.
[17] M.R. Khosravani, M. Silani, K. Weinberg, Fracture studies of ultra-high performance concrete using dynamic Brazilian tests, Theor. Appl. Fract. Mech. 93 (2018) 302–310. https://doi.org/10.1016/j.tafmec.2017.10.001.
[18] J. López, P. Serna, J. Navarro-Gregori, E. Camacho, An inverse analysis method based on deflection to curvature transformation to determine the tensile properties of UHPFRC, Mater. Struct. 48 (2015) 3703–3718. https://doi.org/10.1617/s11527-014-0434-0.
[19] T. Soetens, S. Matthys, Different methods to model the post-cracking behaviour of hooked-end steel fibre reinforced concrete, Constr. Build. Mater. 73 (2014) 458–471. https://doi.org/10.1016/j.conbuildmat.2014.09.093.
[20] D. Lange-Kornbak, B. Karihaloo, Tension softening of short-fibre-reinforced cementitious composites, Cem. Concr. Compos. 19 (4) (1997) 315–328. https://doi.org/10.1016/S0958-9465(97)00027-9.
[21] D. Yoo, N. Banthia, Mechanical properties of ultra-high-performance fiber-reinforced concrete: a review, Cem. Concr. Compos. 73 (2016) 267–280. https://doi.org/10.1016/j.cemconcomp.2016.08.001.
[22] D. Yoo, S. Kim, J. Park, Comparative flexural behavior of ultra-high-performance concrete reinforced with hybrid straight steel fibers, Constr. Build. Mater. 132 (2017) 219–229. https://doi.org/10.1016/j.conbuildmat.2016.11.104.
[23] L. Evans, L. Margetts, V. Casalegno, F. Leonard, T. Lowe, P. Lee, M. Schmidt, P. Mummery, Thermal characterisation of ceramic/metal joining techniques for fusion applications using X-ray tomography, Fusion Eng. Des. 89 (6) (2014) 826–836. https://doi.org/10.1016/j.fusengdes.2014.05.002.
[24] T. Marrow, L. Babout, A. Jivkov, P. Wood, D. Engelberg, N. Stevens, P. Withers, R. Newman, Three dimensional observations and modelling of intergranular stress corrosion cracking in austenitic stainless steel, J. Nucl. Mater. 352 (1–3) (2006) 62–74. https://doi.org/10.1016/j.jnucmat.2006.02.042.
[25] A. Hillerborg, M. Modéer, P. Petersson, Validation of X-ray microfocus computed tomography as an imaging tool for porous structures, Rev. Sci. Instrum. 79 (1) (2008) 013711. https://doi.org/10.1063/1.2838584.
[26] P. Wright, X. Fu, I. Sinclair, S. Spearing, Ultra high resolution computed tomography of damage in notched carbon fiber-epoxy composites, J. Compos. Mater. 42 (19) (2008) 1993–2002. https://doi.org/10.1177/0021998308092211.
[27] P.J. Schilling, B.R. Karedla, A.K. Tatiparthi, M.A. Verges, P.D. Herrington, X-ray computed microtomography of internal damage in fiber reinforced polymer matrix composites, Compos. Sci. Technol. 65 (14) (2005) 2071–2078. https://doi.org/10.1016/j.compscitech.2005.05.014.
[28] X. Huining, T. Yiqiu, Y. Xingao, X-ray computed tomography in hydraulics of asphalt mixtures: procedure, accuracy, and application, Constr. Build. Mater. 108 (2016) 10–21. https://doi.org/10.1016/j.conbuildmat.2016.01.032.
[29] F. Farhat, D. Nicolaides, A. Kanellopoulos, B.L. Karihaloo, High performance fibre-reinforced cementitious composite (CARDIFRC) - performance and application to retrofitting, Eng. Fract. Mech. 74 (1–2) (2007) 151–167. https://doi.org/10.1016/j.engfracmech.2006.01.023.
[30] T. Suzuki, H. Ogata, R. Takada, M. Aoki, M. Ohtsu, Use of acoustic emission and X-ray computed tomography for damage evaluation of freeze-thawed concrete, Constr. Build. Mater. 24 (12) (2010) 2347–2352. https://doi.org/10.1016/j.conbuildmat.2010.05.005.
[31] A. du Plessis, B.J. Olawuyi, W.P. Boshoff, S.G. le Roux, Simple and fast porosity analysis of concrete using X-ray computed tomography, Mater. Struct. 49 (1–2) (2016) 553–562. https://doi.org/10.1617/s11527-014-0519-9.
[32] Z. Yang, W. Ren, R. Sharma, S. McDonald, M. Mostafavi, Y. Vertyagina, T. Marrow, In-situ X-ray computed tomography characterisation of 3D fracture evolution and image-based numerical homogenisation of concrete, Cem. Concr. Compos. 75 (2017) 74–83. https://doi.org/10.1016/j.cemconcomp.2016.10.001.
[33] Z.W. Yu, S. Tan, Z. Shan, X. Tian, X-ray computed tomography quantification of damage in concrete under compression considering irreversible mode-II microcracks, Fatigue Fract. Eng. Mater. Struct. 40 (12) (2017) 1960–1972. https://doi.org/10.1111/ffe.12611.
[34] J.-P. Suuronen, A. Kallonen, M. Eik, J. Puttonen, R. Serimaa, H. Herrmann, Analysis of short fibres orientation in steel fibre-reinforced concrete (SFRC) by X-ray tomography, J. Mater. Sci. 48 (3) (2013) 1358–1367. https://doi.org/10.1007/s10853-012-6882-4.
[35] A.C. Bordelon, J.R. Roesler, Spatial distribution of synthetic fibers in concrete with X-ray computed tomography, Cem. Concr. Compos. 53 (2014) 35–43. https://doi.org/10.1016/j.cemconcomp.2014.04.007.
[36] H. Herrmann, E. Pastorelli, A. Kallonen, J.-P. Suuronen, Methods for fibre orientation analysis of X-ray tomography images of steel fibre reinforced concrete (SFRC), J. Mater. Sci. 51 (8) (2016) 3772–3783. https://doi.org/10.1007/s10853-015-9695-4.
[37] G.L. Balázs, O. Czoboly, E. Lublóy, K. Kapitány, A. Barsi, Observation of steel fibres in concrete with computed tomography, Constr. Build. Mater. 140 (2017) 534–541. https://doi.org/10.1016/j.conbuildmat.2017.02.114.
[38] T. Ponikiewski, J. Katzer, M. Bugdol, M. Rudzki, X-ray computed tomography harnessed to determine 3D spacing of steel fibres in self compacting concrete (SCC) slabs, Constr. Build. Mater. 74 (2015) 102–108. https://doi.org/10.1016/j.conbuildmat.2014.10.024.
[39] T. Nguyen, A. Ghazlan, A. Kashani, S. Bordas, T. Ngo, 3D meso-scale modelling of foamed concrete based on X-ray computed tomography, Constr. Build. Mater. 188 (2018) 583–598. https://doi.org/10.1016/j.conbuildmat.2018.08.085.
[40] L. Skarżyński, J. Suchorzewski, Mechanical and fracture properties of concrete reinforced with recycled and industrial steel fibers using digital image correlation technique and X-ray micro computed tomography, Constr. Build. Mater. 183 (2018) 283–299. https://doi.org/10.1016/j.conbuildmat.2018.06.182.
[41] A. Qsymah, R. Sharma, Z. Yang, L. Margetts, P. Mummery, Micro X-ray computed tomography image-based two-scale homogenisation of ultra high performance fibre reinforced concrete, Constr. Build. Mater. 130 (2017) 230–240. https://doi.org/10.1016/j.conbuildmat.2016.09.020.
[42] B. Huang, Q. Li, S. Xu, W. Liu, H. Wang, Fatigue deformation behavior and fiber failure mechanism of ultra-high toughness cementitious composites in compression, Mater. Des. 157 (2018) 457–468. https://doi.org/10.1016/j.matdes.2018.08.002.
[43] J. Wuest, E. Denarié, E. Brühwiler, L. Tamarit, M. Kocher, E. Gallucci, Tomography analysis of fiber distribution and orientation in ultra high-performance fiber-reinforced composites with high-fiber dosages, Exp. Tech. 33 (5) (2009) 50–55. https://doi.org/10.1111/j.1747-1567.2008.00420.x.
[44] Fde Larrard, T. Sedran, Optimization of ultra-high-performance concrete by the use of a packing model, Cem. Concr. Res. 24 (6) (1994) 997–1009. https://doi.org/10.1016/0008-8846(94)90022-1.
[45] R. Deeb, A. Ghanbari, B. Karihaloo, Development of self-compacting high and ultra high performance concretes with and without steel fibres, Cem.

Concr. Compos. 34 (2012) 185–190. https://doi.org/10.1016/j.cemconcomp.2011.11.001.
[46] EN-12390-3:2009, Testing Hardened Concrete Part 3: Compressive Strength of Test Specimens, AENOR. 2009.
[47] EN-12390-13:2014, Testing Hardened Concrete Part 13: Determination of Secant Modulus of Elasticity in Compression, AENOR. 2014.
[48] J. López, P. Serna, J. Navarro-Gregori, H. Coll, A simplified five-point inverse analysis method to determine the tensile properties of UHPFRC from unnotched four-point bending tests, Compos. Part B 91 (2016) 189–204. https://doi.org/10.1016/j.compositesb.2016.01.026.
[49] RILEM-TCM85, Determination of the fracture energy of mortar and concrete by means of three-point bend tests on notched beams, Mater. Struct. 18 (4) (1985) 287–290. https://doi.org/10.1007/BF02472918.
[50] G. Guinea, J. Planas, M. Elices, Measurement of the fracture energy using three-point bend tests: part 1 - influence of experimental procedures, Mater. Struct. 25 (1992) 212–218. https://doi.org/10.1007/BF02473065.
[51] J. Planas, M. Elices, G. Guinea, Measurement of the fracture energy using three-point bend tests: part 2 - influence of bulk energy dissipation, Mater. Struct. 25 (1992) 305–312. https://doi.org/10.1007/BF02472671.
[52] M. Elices, G. Guinea, J. Planas, Measurement of the fracture energy using three-point bend tests: part 3 - influence of cutting the P-δ tail, Mater. Struct. 25 (1992) 327–334. https://doi.org/10.1007/BF02472591.
[53] H.M. Abdalla, B.L. Karihaloo, A method for constructing the bilinear tension softening diagram of concrete corresponding to its true fracture energy, Mag. Concr. Res. 56 (10) (2004) 597–604. https://doi.org/10.1016/j.conbuildmat.2017.02.114.
[54] R. Kumar, B. Bhattacharjee, Porosity, pore size distribution and in situ strength of concrete, Cem. Concr. Res. 33 (2003) 155–164. https://doi.org/10.1016/S0008-8846(02)00942-0.
[55] T. Ponikiewski, J. Katzer, M. Budgol, M. Rudzki, Determination of 3D porosity in steel fibre reinforced SCC beams using X-ray computed tomography, Constr. Build. Mater. 68 (2014) 333–340. https://doi.org/10.1016/j.conbuildmat.2014.06.064.
[56] A. Neville, Properties of Concrete, 5th ed. ed., Pearson Education Limited, England, 2011.
[57] B. Das, B. Kondraivendhan, Implication of pore size distribution parameters on compressive strength, permeability and hydraulic diffusivity of concrete, Constr. Build. Mater. 28 (1) (2012) 382–386. https://doi.org/10.1016/j.\ignorespacesconbuildmat.2011.08.055.
[58] T. Nguyen, H. Bui, T. Ngo, G. Nguyen, Experimental and numerical investigation of influence of air-voids on the compressive behaviour of foamed concrete, Mater. Des. 130 (2017) 103–119. https://doi.org/10.1016/j.matdes.2017.05.054.
[59] D. Yoo, H. Shin, J. Yang, Y. Yoon, Material and bond properties of ultra high performance fiber reinforced concrete with micro steel fibers, Compos. Part B 58 (2014) 122–133. https://doi.org/10.1016/j.compositesb.2013.10.081.
[60] K. Kendall, A.J. Howard, J.D. Birchall, P.L. Pratt, B.A. Proctor, S.A. Jefferis, The relation between porosity, microstructure and strength, and the approach to advanced cement-based materials, Philos. Trans. R. Soc. Lond. Ser. A Math. Phys. Sci. 310 (1983) 139–153. https://doi.org/10.1098/rsta.1983.0073.
[61] J. Fládr, P. Bílý, Specimen size effect on compressive and flexural strength of high-strength fibre-reinforced concrete containing coarse aggregate, Compos. Part B 138 (2018) 77–86. https://doi.org/10.1016/j.compositesb.2017.11.032.
[62] S. Kang, B. Lee, J. Kim, Y. Kim, The effect of fibre distribution characteristics on the flexural strength of steel fibre-reinforced ultra high strength concrete, Constr. Build. Mater. 25 (5) (2011) 2450–2457. https://doi.org/10.1016/j.conbuildmat.2010.11.057.
[63] S. Benson, B. Karihaloo, CARDIFRC - development and mechanical properties. Part III: uniaxial tensile response and other mechanical properties, Mag. Concr. Res. 57 (8) (2005) 433–443. https://doi.org/10.1680/macr.2005.57.8.433.
[64] A.F. Bower, M. Ortiz, The influence of grain size on the toughness of monolithic ceramics, J. Eng. Mater. Technol. 115 (1993) 228–236. https://doi.org/10.1016/j.cemconcomp.2014.04.007.
[65] S. Benson, D. Nicolaides, B. Karihaloo, CARDIFRC - development and mechanical properties. Part II: fibre distribution, Mag. Concr. Res. 57 (7) (2005) 421–432. https://doi.org/10.1680/macr.2005.57.7.421.
[66] B. Karihaloo, Fracture Mechanics and Structural Concrete, Longman. 1995.
[67] J. Ríos, H. Cifuentes, C. Leiva, C. García, M. Alba, Behavior of high-strength polypropylene fiber-reinforced self-compacting concrete exposed to high temperatures, J. Mater. Civ. Eng. (ASCE) 30 (11) (2018) 04018271. https://doi.org/10.1061/(ASCE)MT.1943-5533.0002491.
[68] Y. Su, J. Li, C. Wu, P. Wu, M. Tao, X. Li, Mesoscale study of steel fibre-reinforced ultra-high performance concrete under static and dynamic loads, Mater. Des. 116 (2017) 340–351. https://doi.org/10.1016/j.matdes.2016.12.027.
[69] W. Alyhya, M.A. Dhaheer, M. Al-Rubaye, B. Karihaloo, Influence of mix composition and strength on the fracture properties of self-compacting concrete, Constr. Build. Mater. 110 (2016) 312–322. https://doi.org/10.1016/j.conbuildmat.2016.02.037.
[70] K. Park, G.H. Paulino, J. Roesler, Cohesive fracture model for functionally graded fiber reinforced concrete, Cem. Concr. Res. 40 (2010) 956–965. https://doi.org/10.1007/BF02472671.
[71] A. Hillerborg, M. Modéer, P. Petersson, Analysis of crack formation and crack growth in concrete by means of fracture mechanics and finite elements, Cem. Concr. Res. 6 (6) (1976) 773–781. https://doi.org/10.1016/0008-8846(76)90007-7.
[72] H. Cifuentes, B. Karihaloo, Determination of size-independent specific fracture energy of normal- and high-strength self-compacting concrete from wedge splitting tests, Constr. Build. Mater. 48 (2013) 548–553. https://doi.org/10.1016/j.conbuildmat.2013.07.062.